Experimental and Modeling Approach to Decolorization of Azo Dyes by Ultrasound: Degradation of the Hydrazone Tautomer

Alimet Sema Özen and Viktorya Aviyente*

Department of Chemistry, Boğaziçi University, 34342 Bebek, Istanbul, Turkey

Gökçe Tezcanli-Güyer and Nilsun H. Ince

Institute of Environmental Sciences, Boğaziçi University, 34342, Bebek, Istanbul, Turkey

Received: August 11, 2004; In Final Form: January 12, 2005

Sonochemical bleaching of monoazo dyes C.I. Acid Orange 7 and C.I Acid Orange 8, which exist in their hydrazone forms in dye solutions, was investigated by irradiating 40 μM dye solutions using a 300 kHz emitter. It was found that the rate of bleaching was first-order with respect to the maximum absorption of the dye in the visible band and accelerated with increased acidity. Decolorization of Acid Orange 7 was slightly faster than that of Acid Orange 8 at equivalent test conditions. The oxidative degradation of Acid Orange 7 and Acid Orange 8 were modeled by means of density functional theory calculations. The adduct formation by hydroxyl radical attack to the carbon atom bearing the azo linkage was more preferred over the attack on the nitrogen atom. A competing reaction of hydrogen abstraction from the CH_3 group in C.I Acid Orange 8 was found responsible for the difference in color removal rates.

Introduction

The presence of unfixed azo dye residuals in textile industry wastewater has been a primary environmental problem not only because these dyes are relatively resistant to conventional treatment methods, but also because some of them produce carcinogenic amines as byproducts of hydrolysis. This challenge seems to be resolved by the introduction of advanced oxidation processes (AOP),[1−5] where highly reactive hydroxyl radicals generated chemically (Fenton's reagent), photochemically (UV/TiO_2/H_2O_2, O_3/UV), and by radiolytic or sonolytic means are used as oxidizing agents for the bleaching and mineralization of troublesome waste. During sonication of a liquid, water vapor and dissolved gases are entrapped by cavitation bubbles, which expand at rarefaction cycles of the bubbles and release extreme temperatures upon adiabatic collapse.[6,7] Under these conditions, bubble contents are pyrolytically fragmented into radical species, some of which diffuse into the aqueous phase to initiate a series of oxidation reactions called "sonochemistry".[2] The main chain reactions occurring during collapse of a bubble are shown below:

$$H_2O +))) \rightarrow {}^{\bullet}OH + {}^{\bullet}H \text{ (pyrolysis)}$$

$${}^{\bullet}OH + {}^{\bullet}H \rightarrow H_2O$$

$${}^{\bullet}OH + {}^{\bullet}OH \rightarrow H_2O_2$$

$$2{}^{\bullet}OH \rightarrow H_2O + O$$

In water and wastewater treatment practices, organic pollutants may be destroyed either (i) in the cavitation bubble itself by pyrolytic decomposition (if the compounds are hydrophobic), (ii) at the interfacial sheath between the gaseous bubble and the surrounding liquid, or (iii) in the solution bulk via oxidative degradation by hydroxyl radicals. The extent of oxidation in bulk liquid is limited by the quantity of hydroxyl radicals diffused into the water.

The chromophore structure of azo dyes is made of two aryl rings connected through an azo, −N=N−, bridge.[8] The presence of at least one protic donor group in conjugation to this azo bridge leads to a prototropic equilibrium that is generally referred as the azo-hydrazone tautomerism (**1**).[8−11]

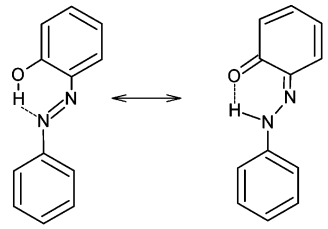

(1)

The main reactions of hydroxyl radicals with azo compounds can therefore be addition to the chromophore, addition to the aryl rings, hydrogen abstraction, or one-electron oxidation.[3] Experimentally proposed degradation mechanisms focus on the cleavage of either the N−N bond resulting in nitrosoaryl intermediates or the C−N bond with generation of benzene as one of the intermediate products (**2**).[12−13]

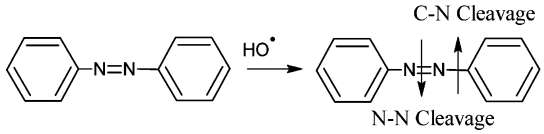

(2)

In previous studies,[14,15] addition reactions were modeled using density functional theory calculations and it was found that bleaching of the dye occurs through the cleavage of the N−N bond rather than the cleavage of the C−N bond in the case of azo tautomer. It was concluded that the presence of the

* Author to whom correspondence should be addressed.

10.1021/jp046374m CCC: $30.25
Published on Web 03/24/2005

hydrazone tautomer in experimental studies, rather than the azo tautomer, could be indicative for the mechanism involving C−N bond cleavage.[14] Moreover, hydrogen abstraction and addition to the ring reactions were competing with bond cleavage through addition reactions.[15]

The present study is an attempt to combine experimental and computational efforts to elucidate the oxidative cleavage reaction mechanism of the hydrazone tautomers. The azo dyes C.I. Acid Orange 7 (**AO7**) and C.I. Acid Orange 8 (**AO8**), that are known to exist preferably in their hydrazone forms (**3**) in the dye

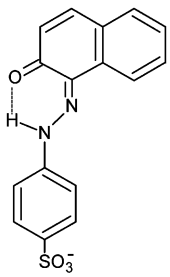

C.I. Acid Orange 7

(Orange II)

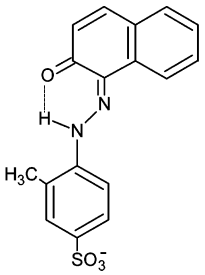

C.I. Acid Orange 8

(3)

solutions,[16−18] have been selected for this purpose. Modeling of the reactive pathways for the reactions of hydroxyl radical with hydrazone tautomer has been performed using density functional theory (DFT) calculations to investigate the most plausible mechanism for the initial radical attack that might further result in bond cleavage. The aim of the Experimental Section was to examine the degradation of the two dyes by 300 kHz ultrasonic irradiation at acidic and near acidic pH and to assess the impacts of dye structure on the rate of the color decay. It is also intended to explain the difference in the rates of color decay by modeling of the competing reactive pathways using DFT methods.

Methodology

Experimental. *Test Dyes and Sample Preparation.* The test dyes AO7 and AO8 were obtained from Aldrich in 85% and 65% purity, respectively, and used as received. All other reagents were analytical Merck grade. Stock dye solutions were prepared by dissolving 1 g of each dye in 1 L of ultrapure deionized water. Test solutions were made by diluting the stocks to 40 μM followed by aeration for 1 h.

Experimental Setup and Procedure. The experimental system consisted of a 150-mL glass cell surrounded by a water-cooling jacket to keep its contents at constant temperature (20 ± 0.5 °C), a plate type piezoelectric transducer emitting ultrasonic waves at 300 kHz, and a 25 W generator to convert electrical power input into mechanical energy (Undatim Ultrasonics, Belgium). The active acoustical vibrational area of the transducer was 22 cm^2. The irradiation intensity in the reactor was 0.184 W/mL as determined by calorimetry.[7]

One hundred milliliter aliquots of aerated test samples were irradiated for 1 h during argon bubbling at 1 L/min under the following conditions: (i) without any pH adjustment (upon dissolution, both dyes were slightly acidic with pH = 6.10 in AO7 and 5.95 in AO8) and (ii) after the addition of 10 N H_2SO_4 (0.05 mL) to adjust pH to 3. Effluent samples were collected at 0, 3, 5, 7, 10, 15, 20, 25, 30, 45, and 60 min of contact for spectrophotometric analysis.

Analytical. The absorption spectra of raw and sonicated samples were monitored at 200−800 nm and at the visible absorption of the solutions using a Unicam, Helios Alpha/Beta double-beam spectrophotometer through a 1-cm path length.

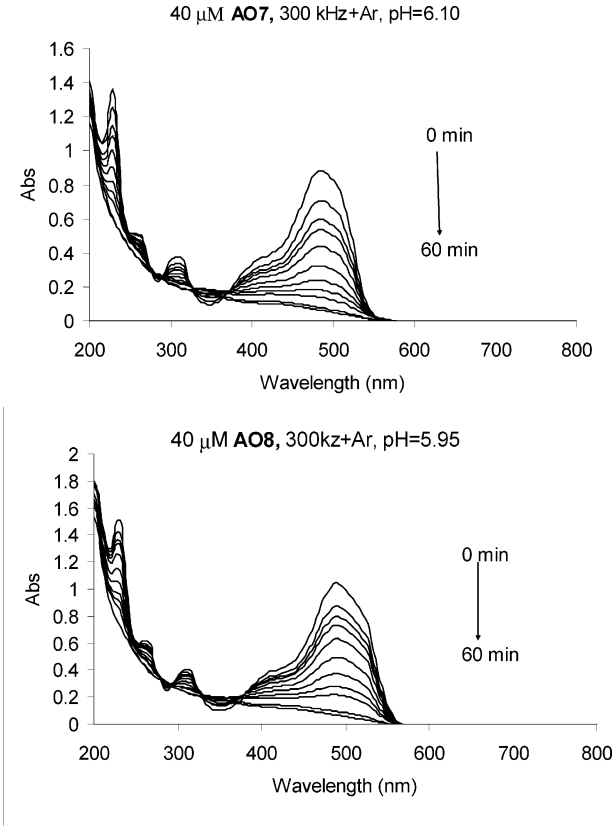

Figure 1. Spectral changes during 1-h sonication of 40 mM dye solutions under nonbuffered conditions.

Computational. The Gaussian98[19] program system has been employed for the calculation of geometries and energies. Optimizations were performed at MPW1K/6-31G(d) level of theory. Energies are further refined with single-point calculations at MPW1K/6-31+G(d,p) level. Ground-state and transition-state structures have been confirmed by frequency analyses. Transition structures have been characterized by having one imaginary frequency that belonged to the reaction coordinate, corresponding to a first-order saddle point. Zero-point vibrational energies (ZPEs) have been added (unless otherwise stated) but not scaled since they would only be used for comparative purposes. IRC calculations have been performed for all of the transition geometries, and corresponding minima have been confirmed. Continuum solvent effects were modeled using the integral equation formalism (IEF) polarized continuum model (PCM) of Tomasi et al.[21] within self-consistent reaction field (SCRF) theory, by means of single-point calculations based on the gas-phase geometries. To gain better insight into the specific solute−solvent interactions, a supermolecule approach has been adopted by adding one explicit water molecule to the reactive region throughout the reaction paths of AO8.

Results and Discussion

A. Ultrasonic Dye Degradation. Comparable profiles of the dye spectra (C_0 = 40 μM) at nonbuffered and acid-buffered conditions before and during sonication are presented in Figures 1 and 2, respectively. The obvious absorption peak at 488 nm in the spectrum of **AO7** and at 492 nm in the spectrum of **AO8** implies the preference of the hydrazone tautomer even though there are very small shoulders around 400−420 nm because of the azo tautomer. Overall, these shoulders are negligible. Azo

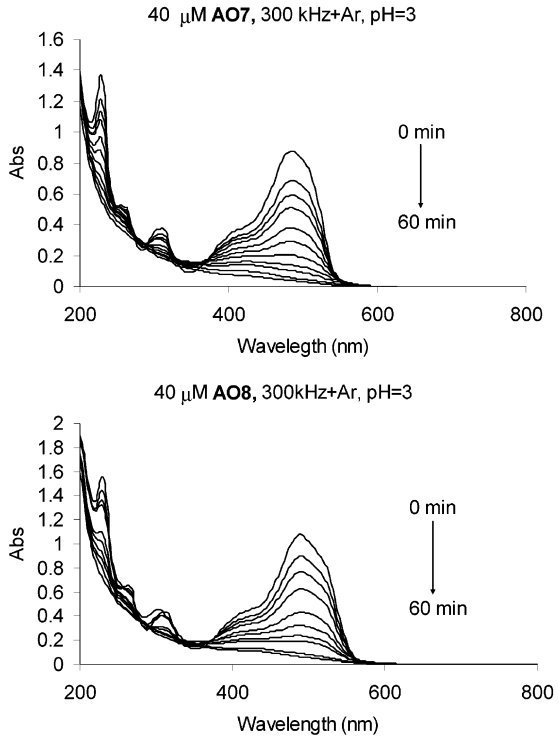

Figure 2. Spectral changes during 1-h sonication of 40 mM dye solutions under acidic conditions.

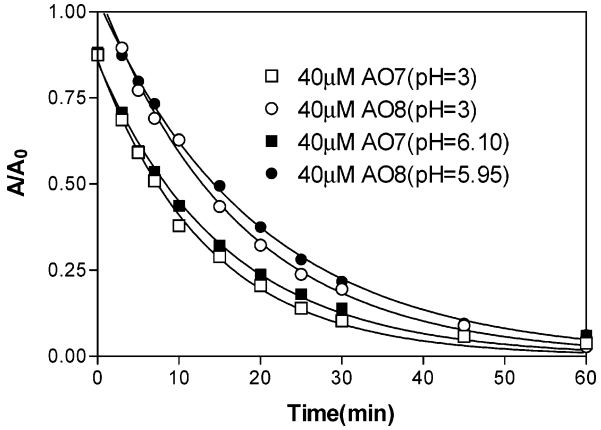

Figure 3. Comparative rates of visible absorption abatement in dye solutions. The solid lines represent the fit of experimental data to $A/A_0 = e^{-kt}$.

TABLE 1: First-Order Bleaching Rate Constants for AO7 and AO8

dye	pH	$10^{-3} \times k$ (min^{-1})	r^2
AO7	3	74.02 ± 2.42	0.99
AO7	6.10	64.09 ± 2.58	0.99
AO8	3	58.60 ± 1.41	0.99
AO8	5.95	50.92 ± 0.77	0.99

forms absorb typically at 400−440 nm, whereas hydrazone forms absorb at 475−510 nm.[22]

The main reaction pathway for sonicated azo dye solutions is oxidation by hydroxyl radical attack in the bulk liquid. Thermal or oxidative reactions may also occur at the bubble−liquid interface depending on the degree of pollutant's partitioning between gaseous and aqueous interfaces.[23]

The rate of color decay followed pseudo-first-order kinetics with respect to the visible absorption of the dyes:

$$-\frac{dA}{dt} = k'A \tag{4}$$

where A is the maximum absorbance of the dye solution in the visible band at time t and k' is the first-order absorbance decay coefficient (time^{-1}). Profiles of color degradation during 1-h sonication of the test solutions and the fit of the data to the integrated or exponential form of eq 4 are presented in Figure 3. Estimated first-order sonochemical bleaching rate constants for the two dyes are presented in Table 1.

The hydroxyl group in ortho position to the azo bond in both test dyes favors the hydrazone against the azo structure. Relatively rapid decolorization of the dyes can be attributed to the additional reactivity of hydrazone forms with secondary radicals such as $^{\bullet}HO_2/^{\bullet}O_2$ (in addition to reaction with hydroxyl radicals). Although these secondary radicals are less powerful than $^{\bullet}$OH as oxidizing agents, they are more stable and unlike $^{\bullet}$OH may accumulate in the aqueous phase.

Under nonbuffered and acidic conditions, decolorization of **AO7** is faster than that of **AO8**. Competing reactions such as hydrogen abstraction due to ortho-CH_3 substitution in **AO8** probably decelerated its bleaching. It was found that rate of color decay in both dyes was accelerated by acidification (pH = 3). This result can be attributed to the neutralization of both dyes upon protonation of negatively charged SO_3^- sites and enhanced reactivity because of their hydrophobic enrichment. Acidic conditions are believed to enhance the probability of the dyes to approach the negatively charged cavity bubbles, where $^{\bullet}$OH radicals are most abundant and undergo additional oxidation/pyrolysis degradation at the gas−liquid interface. Similar findings were published in our previous works[17,24]

B. Computational Modeling. *Hydroxyl Radical Addition to Acid Orange 7.* Hydroxyl radicals can add to the −N═C− double bond of the hydrazone tautomer either by bond formation through the nitrogen atom (N-attack) or carbon atom (C-attack) leading to the further cleavage of this bond.

N-attack Pathway. Potential energy surface (PES) and optimized geometries of the nitrogen attack pathway are shown in Figures 4 and 5, respectively. Acid Orange 7 (**AO7**) molecule is planar because of hydrogen bonding between oxygen at the ortho position to the azo link and proton attached to the azo nitrogen. An atoms-in-molecules (AIM) analysis[25] of this molecule was performed in a recent work.[26] Hydroxyl radical forms a pre-reaction complex, **AO7−N1**, with Acid Orange 7 by means of π-H interaction with a gain of 4.1 kcal/mol in the system's energy in the gas phase. This energy gain by complex formation is much less in water. The radical addition to the C−N double-bond reaction proceeds through the transition-state **AO7−NTS** with an activation barrier of 10.2 kcal/mol in the gas phase and of 8.7 kcal/mol in water because of solvent stabilization. In the transition state, oxygen−nitrogen interactions occur at a distance of 1.729 Å and the intramolecular hydrogen bonding in the parent molecule is preserved with a slight increase of 0.048 Å in the bond distance. The initial N-attack reaction is endoenergetic by 4.6 kcal/mol in a vacuum, probably because of the loss of this intramolecular hydrogen bonding in the adduct, **AO7−N2**, where hydrogen bond distance in the parent molecule increases to 2.164 Å and planarity is lost. However, the same pathway is exoenergetic in continuum by 3.9 kcal/mol. The solvent stabilization trend complies with the change in the dipole moments going from transition state (23.4 D) to adduct (26.3 D).

C-Attack Pathway. Potential energy surface (PES) and optimized geometries of the carbon attack pathway are shown in Figures 6 and 7, respectively.

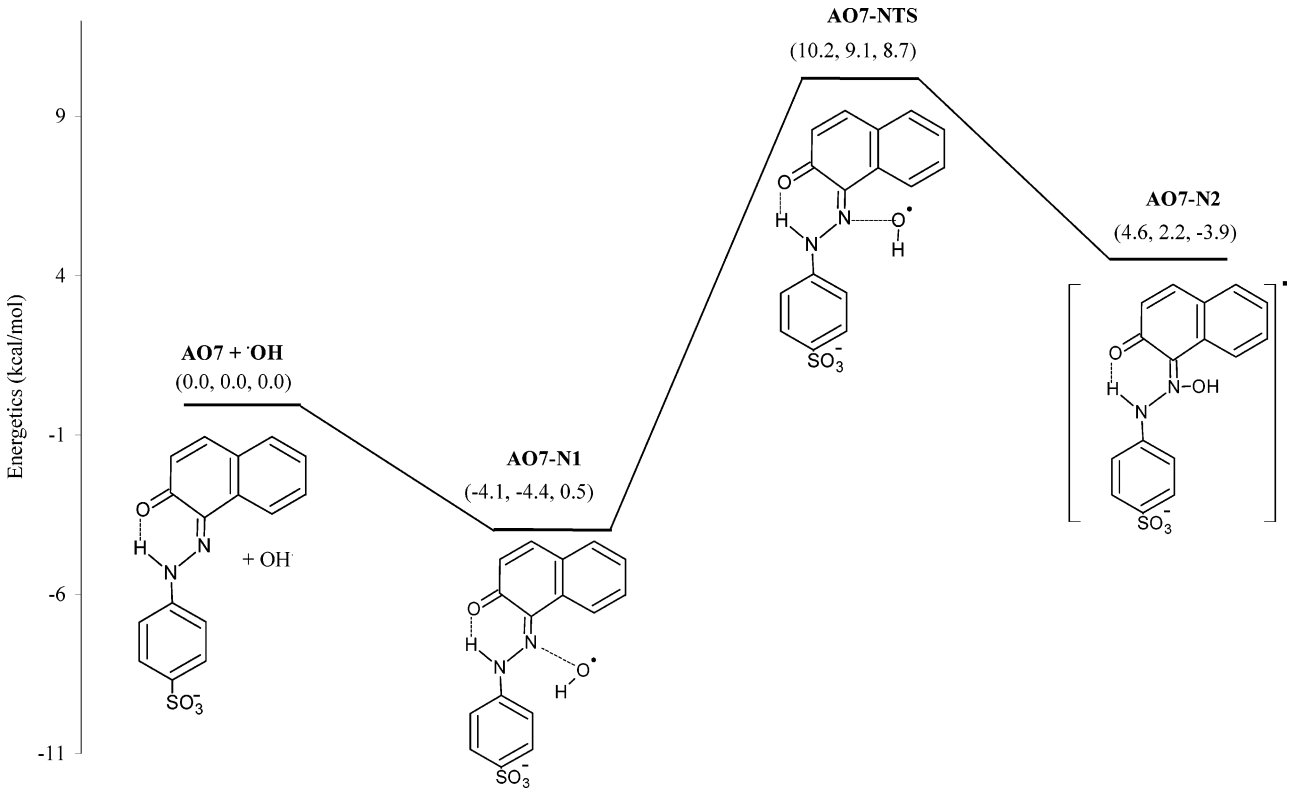

Figure 4. Potential energy profile for N-attack pathway of Acid Orange 7 at MPW1K/6-31G(d) level. Relative energies in parentheses are in the format of (MPW1K/6-31G(d), MPW1K/6-31+G(d,p)//MPW1K/6-31G(d), IEFPCM) values. (0.0 kcal/mol on the relative energy axis corresponds to **AO7** + •OH = (−1500.023062, −1500.356061, −1500.379549) Hartrees with the same format.)

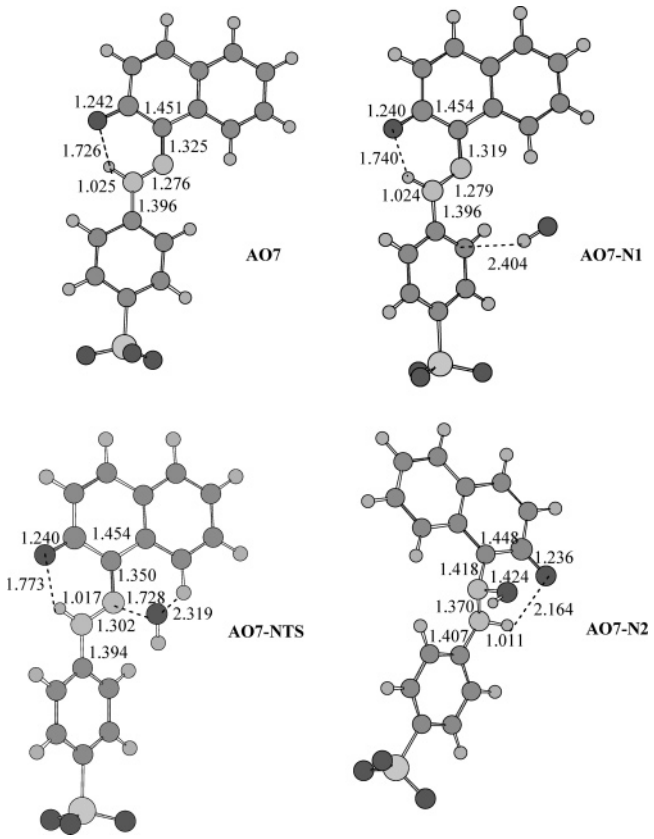

Figure 5. MPW1K/6-31G(d) optimized structures for **AO7** N-attack pathway.

In carbon attack pathway, as it is commonly observed in many radical reactions, a pre-reaction complex (**AO7**−**C1**) forms during the hydroxyl radical addition, through intermolecular hydrogen bonding between hydrogen of the radical and nitrogen of the azo link. As one goes from reactants to the transition-state structure **AO7**−**CTS**, the potential energy profile is quite shallow and the reaction can be considered as barrierless both in the gas phase and in water. Adduct formation is exoenergetic by 24.6 kcal/mol in the gas phase. The formation of an intramolecular hydrogen bond network can be the reason for the stabilization of the adduct **AO7**−**C2**. Further stabilization of 30.8 kcal/mol in the dielectric continuum might be explained, again, by the change in the dipole moments of the TS (**AO7**−**CTS** 22.5 D) and adduct (**AO7**−**C2** 26.8 D).

The same trend in energetics has also been observed for both radical attack pathways by the refinement of energy at the MPW1K/6-31+G(d,p)//MPW1K/6-31G(d) level of theory.

*Comparison of the Potential Energy Surfaces for **AO7**.* DFT calculations in a vacuum represent the reaction of dye with hydroxyl radical in the cavity bubble or on the interface during sonication, and continuum calculations represent the same reaction in the bulk solution. As it can be concluded by comparison of Figures 4 and 6, barrierless C-attack pathway is preferred over the N-attack pathway, with an activation energy of 9.1 kcal/mol, in the hydroxyl radical reactions with hydrazone tautomer of azo dyes. Initial attack and adduct formation are important steps in the course of the reaction in terms of consumption of the hydroxyl radicals in the reaction environment. Therefore, once the adduct structure is determined, this information can further be used to predict the final cleavage products.

HPLC, GC-MS, and capillary electrophoresis (CE-MS and CE-UV/DAD) analyses have given mainly two intermediates for Acid Orange 7 advanced oxidation degradation by different methods: 4-hydroxybenzenesulfonic acid and 1,2-naphthaquinone (or 1,2-dihydroxy naphthalene) (Figure 8).[1,27−28] These intermediates might be indicative of a possible attack on the C

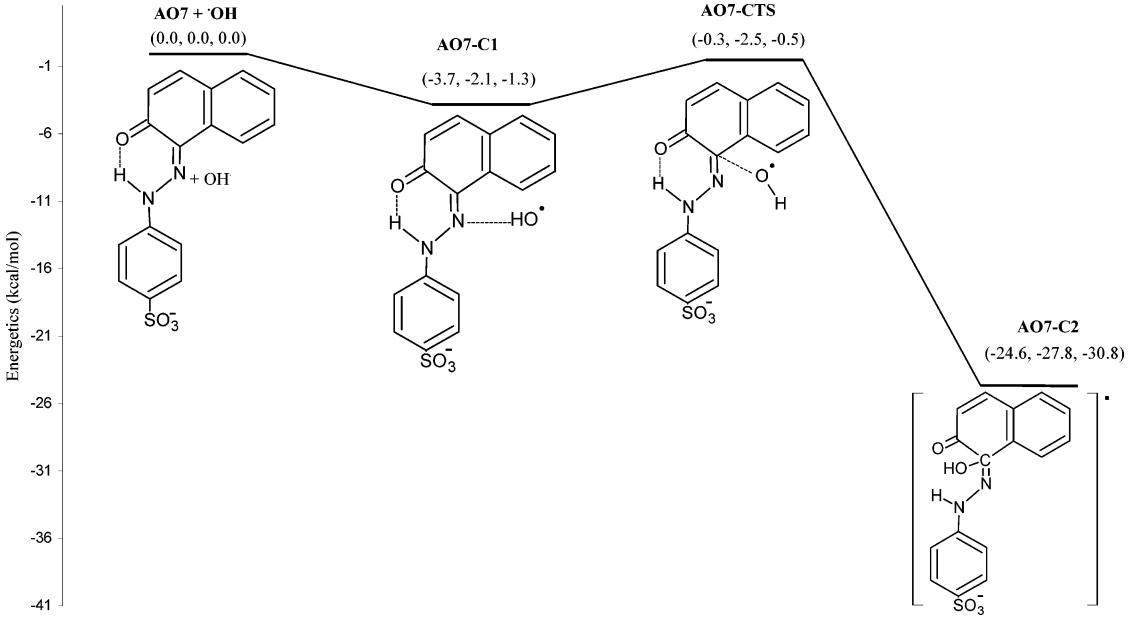

Figure 6. Potential energy profile for C-attack pathway of Acid Orange 7 at MPW1K/6-31G(d) level. Relative energies in parentheses are in the format of (MPW1K/6-31G(d), MPW1K/6-31+G(d,p)//MPW1K/6-31G(d), IEFPCM) values. (0.0 kcal/mol on the relative energy axis corresponds to **AO7** + ·OH = (−1500.023062, −1500.356061, −1500.379549) Hartrees with the same format.)

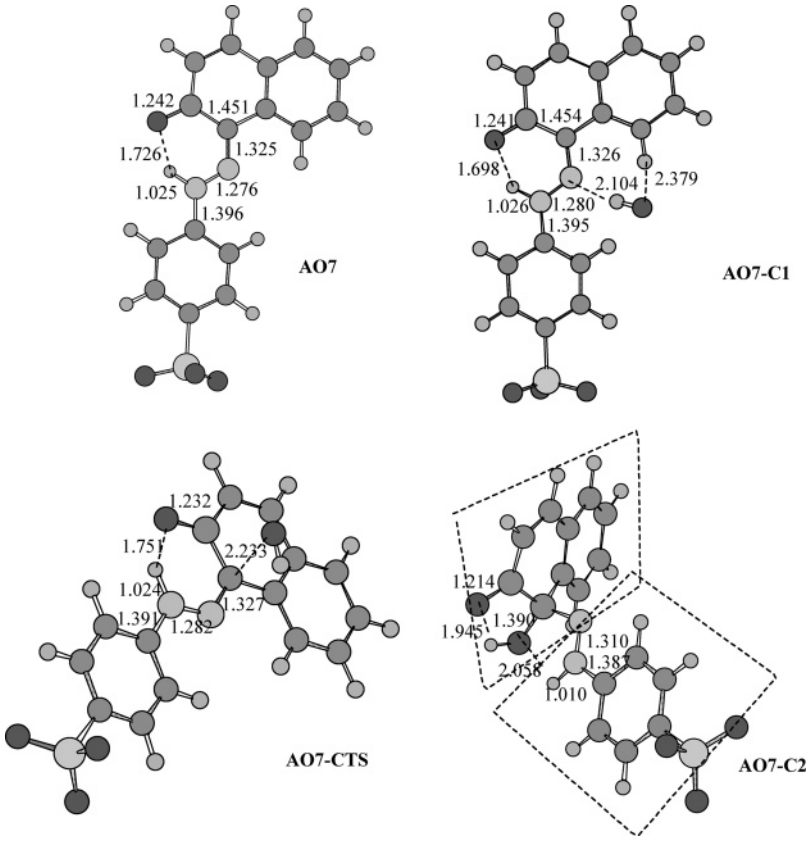

Figure 7. Optimized structures for **AO7** C-attack pathway.

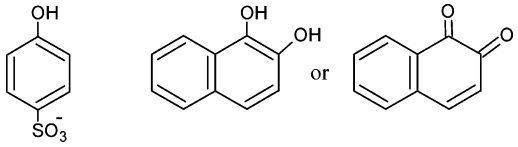

Figure 8. Intermediate structures identified during the advanced oxidation of Acid Orange 7.[1,27,28]

rather than the N, which is in accord with the findings of the present study. Further modeling of the adduct cleavage might be a proposal for future work as a support for the arguments discussed here.

*Molecular Structure Factors Controlling the Color Decay: **AO7** vs **AO8**.* The present section aims to explain the difference in the color decay rates of **AO7** and **AO8**, as shown in Table 1 in the ultrasonic dye degradation section, by means of quantum mechanics.

Hydroxyl Radical Addition to Acid Orange 8. Potential energy surfaces (PES) of the nitrogen and carbon attack pathways for **AO8** are shown in Figures 9 and 10, respectively. Optimized

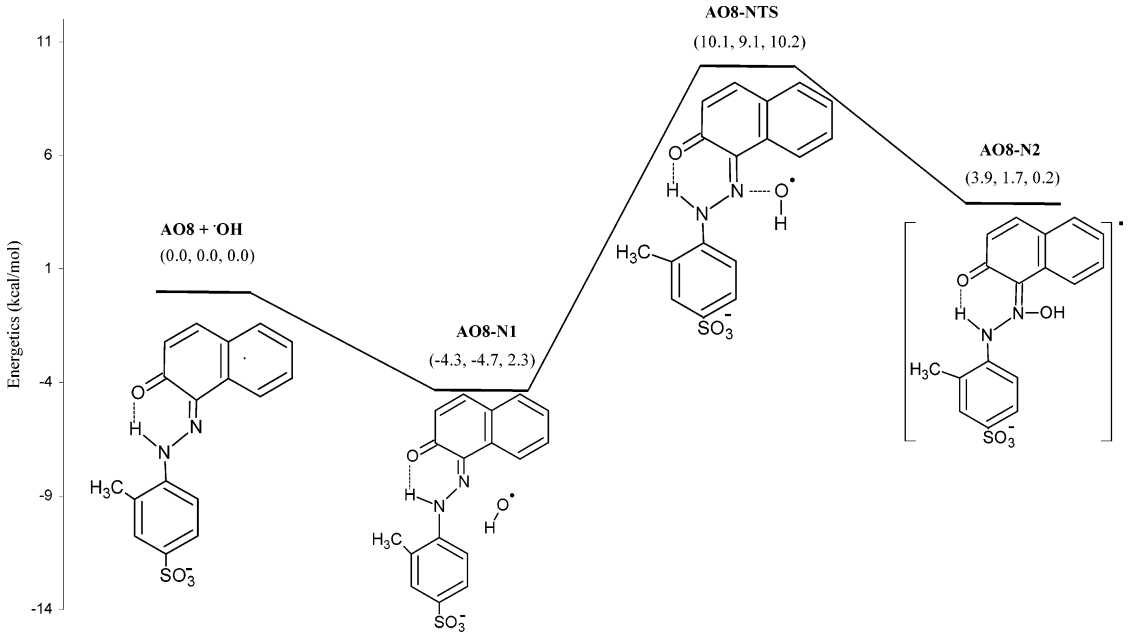

Figure 9. Potential energy profile for N-attack pathway of Acid Orange 8 at MPW1K/6-31G(d) level. Relative energies in parentheses are in the format of (MPW1K/6-31G(d), MPW1K/6-31+G(d,p)//MPW1K/6-31G(d), IEFPCM) values. (0.0 kcal/mol on the relative energy axis corresponds to **AO8** + ·OH = (−1539.303765, −1539.667696, −1539.694109) Hartrees with the same format.)

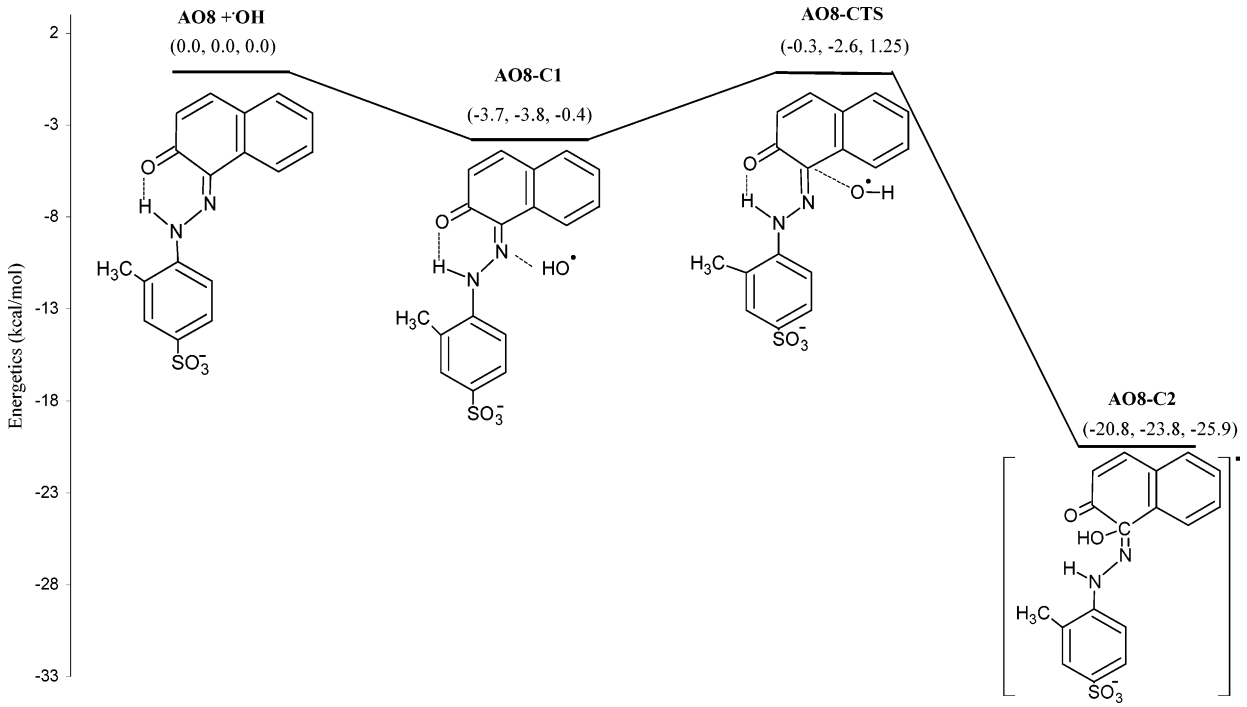

Figure 10. Potential energy profile for C-attack pathway of Acid Orange 8 at MPW1K/6-31G(d) level. Relative energies in parentheses are in the format of (MPW1K/6-31G(d), MPW1K/6-31+G(d,p)//MPW1K/6-31G(d), IEFPCM) values. (0.0 kcal/mol on the relative energy axis corresponds to **AO8** + ·OH = (−1539.303765, −1539.667696, −1539.694109) Hartrees with the same format.)

geometries are given in Figures 11 and 12. **AO8** molecule is planar because of the intramolecular hydrogen bonding similar to the case of **AO7**. Bond distances are similar for both molecules. However, the hydrogen bond distance decreases to 1.711 Å while it is 1.725 Å in **AO7**. Potential energy surfaces of these azo dyes resemble each other with similar barriers and reaction energies for radical addition. Adduct formation in **AO8** occurs through radical attack of the carbon atom, and the endoenergetic, high-barrier N-attack pathway is quite unfavorable. The exoenergicity of barrierless C-attack pathway in **AO8** drops almost 4 kcal/mol in a vacuum (this is almost equivalent to a weak hydrogen bond energy) probably because of the prevention of the formation of the nice intramolecular hydrogen bond network observed in **AO7**−radical adduct, **AO7**−**C2**, by the bulkiness created by methyl substituent in **AO8**. Now the question arises: if these two compounds, **AO7** and **AO8**, are so similar in geometry and their PESs resemble so strictly each other, then why does their color removal by hydroxyl radicals occur at close yet different rates? The explanation to the difference in reactivity can be attributed to the presence of a

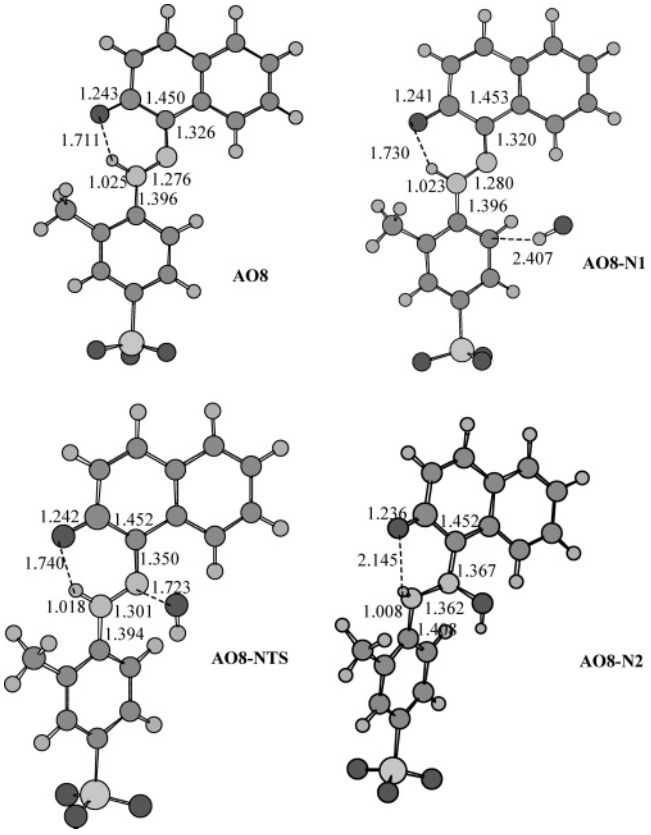

Figure 11. Optimized structures for Acid Orange 8 (**AO8**) N-attack pathway.

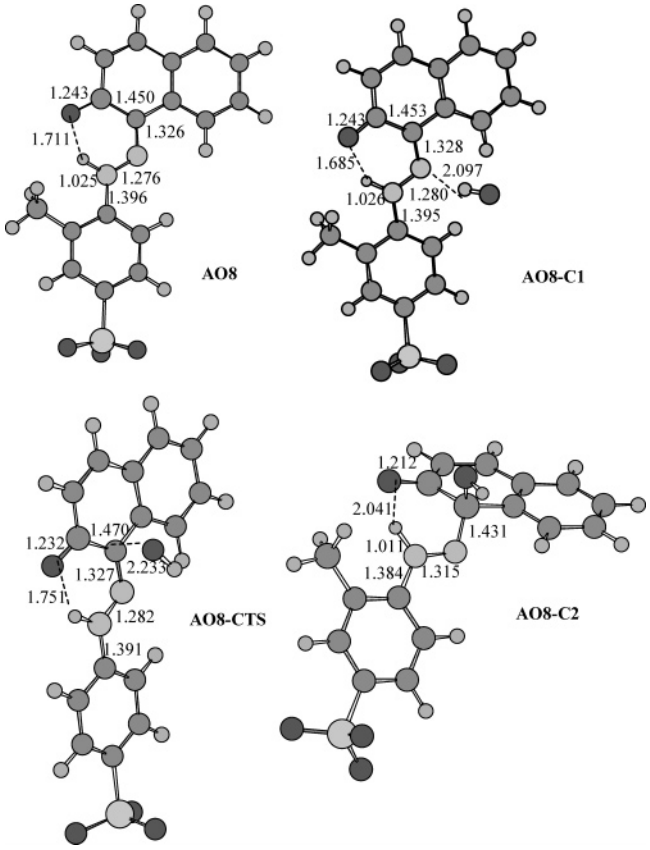

Figure 12. Optimized structures for Acid Orange 8 (**AO8**) C-attack pathway.

competing reaction that would consume the hydroxyl radicals in the case of **AO8** but not in the case of **AO7**, which is a case similar to a previous work with CH_3 substituted dyes.

Competing Reaction for Acid Orange 8: Hydrogen Abstraction versus Addition to Double Bond. As it is mentioned in the Introduction section, hydroxyl radical may abstract hydrogen from organic compounds. It was shown that[15] this reaction competes with the addition reaction especially in the case of CH_3 substitution which provides a better hydrogen donor than the ring carbons. Indeed, the transition state for hydrogen abstraction from the CH_3 group, **AO8**−**HTS**, lies lower in energy than the transition state for C-attack, **AO8**−**CTS**, by 0.7 kcal/mol with MPW1K/6-31G(d) (Figure 13). The stability order of transition states changes in favor of C-attack by 2.2 kcal/mol in continuum and by 1.0 kcal/mol when the energies are refined at a higher level, MPW1K/6-31+G(d,p), but still it is possible to consider a competing reaction to some extent. Moreover, hydrogen abstraction reaction is more exoenergetic than addition reaction by 7.8 kcal/mol in a vacuum even though this difference in reaction energies drops to 2.9 kcal/mol in favor of the addition in the presence of dielectric continuum. These alternating trends in a vacuum and in solvent might be due to characteristics of the cavity used in IEFPCM. In **AO7**, Bondi's atomic radii, which give better results than the default cavity formation method of the Gaussian program, have been employed. Unfortunately, it was not possible to use this option in modeling the C attack pathway of **AO8** because of convergence problems. Therefore, for the sake of convenience, all of the **AO8**-related pathways, namely, N-attack and C-attack radical addition and hydrogen abstraction, were first modeled by the default united atom (UA) model of the program in which hydrogen atoms are enclosed in the sphere of the atom to which they are bonded. However, according to our previous experience,[15] this model is probably overestimating the barriers for hydrogen abstraction reaction from azo dyes because of poor definition of proton interactions. Therefore, to improve the prediction of hydrogen bonds within the intermediates and of proton transfer in the continuum, hydrogen atoms undergoing hydrogen bond type of interactions have been defined explicitly with individual spheres employing the radii from the UFF force field. Indeed, these later calculations (Figure 13) have been comparable to some extra calculations with Bondi's atomic radii, which proposed a barrier height of 2.8 kcal/mol and reaction energy of −27.5 kcal/mol for hydrogen abstraction in solution.

Explicit definition of hydrogen atoms is more important for the reactions where proton transfer occurs than the others. For example, in hydrogen abstraction from **AO8**, by changing the definition of the cavity from UA model to Bondi, a net stabilization of 4.8 and 6.8 kcal/mol has been obtained for activation and reaction energies, respectively. As a comparison with the addition case, the net stabilization for the whole N-attack pathway for **AO8** with the same exchange of methods was only about 0.5−1.5 kcal/mol.

(Energetics for the explicit hydrogen atom definitions of the **AO7** pathways by UFF parameters has been presented as Supporting Information in Table 1S.)

Figure 14 shows the optimized geometry for the pre-reaction complex **AO8**−**H1**, the transition-state **AO8**−**HTS,** and the intermolecular hydrogen-bonded reaction products, **AO8**−**H2** and H_2O_2. Figure 1S represents the potential energy surface for an alternative approach of hydroxyl radical to the methyl group without forming a hydrogen bond with the *o*-oxygen. This latter pathway is slightly unfavorable as compared to the former one. Figure 2S shows the optimized geometries for the alternative hydrogen abstraction transition state and product obtained from IRC calculations.

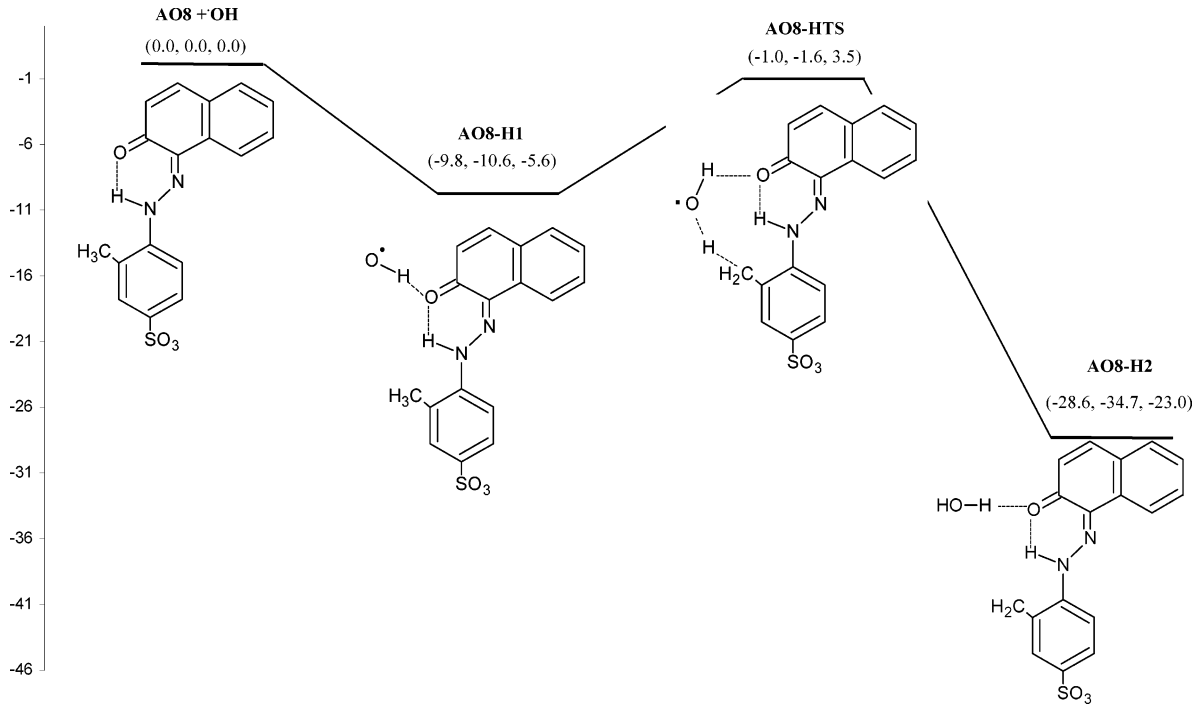

Figure 13. Potential energy profile for hydrogen abstraction pathway of Acid Orange 8 at MPW1K/6-31G(d) level. Relative energies in parentheses are in the format of (MPW1K/6-31G(d), MPW1K/6-31+G(d,p)//MPW1K/6-31G(d), IEFPCM) values. (0.0 kcal/mol on the relative energy axis corresponds to **AO8** + ·OH = (−1539.303765, −1539.667696, −1539.694109) Hartrees with the same format.)

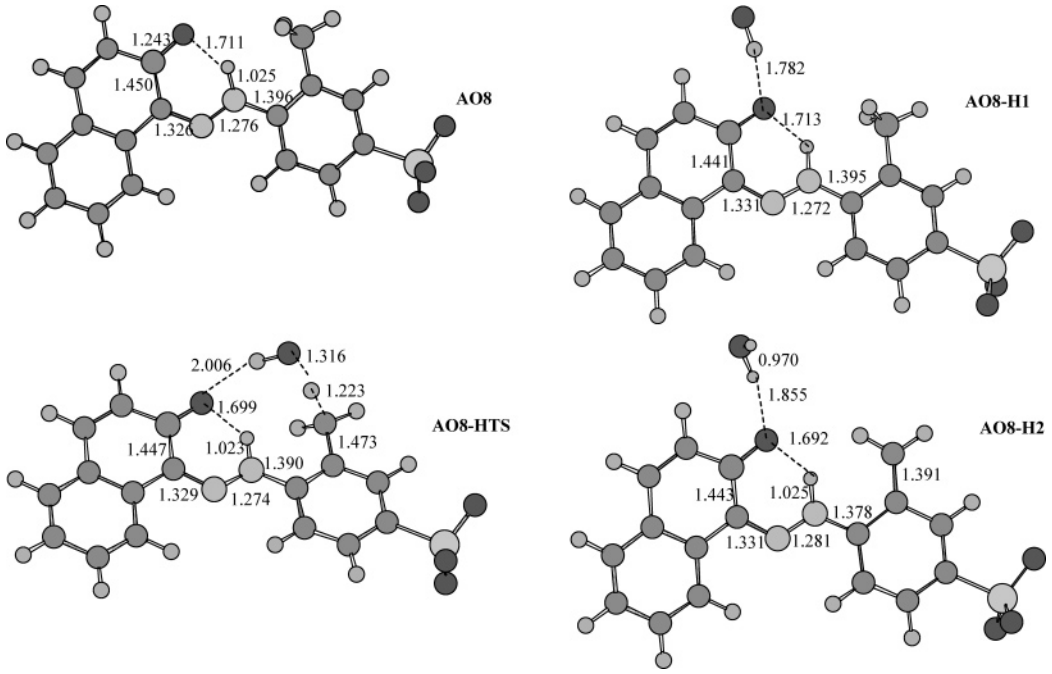

Figure 14. Optimized structures for hydrogen abstraction from CH_3.

To gain better insight into the specific solute−solvent interactions and their effects on the preference of one reactive pathway over the other, especially for the **AO8** cases, a supermolecule approach has been adopted by inclusion of one water molecule forming a complex with the intermediates. In general, addition of an explicit water molecule has had a stabilizing effect in all mechanisms, lowering both the activation barriers and reaction energies. In parallel with the previous cases, N-attack pathway has been the least favored mechanism (Figure 15). On the other hand, the competition between C-attack and hydrogen abstraction mechanisms has become a little bit more prominent by the introduction of water assistance (Figures 16 and 17). In a vacuum, hydrogen abstraction transition state (**AO8W−HTS**) has been more stabilized, and in the continuum now the two transition states, **AO8−HTS** and **AO8W−CTS**, have been located at the same energy level. However, the reaction energies have, again, as in the non-water-assisted mechanism, shown different trends in a vacuum and in continuum, hydrogen abstraction being more favorable in the former by 3.1 kcal/mol and C-attack in the latter by 2.7 kcal/mol. In the water-assisted mechanisms, solvent calculations have been performed by the same method of explicit definition of

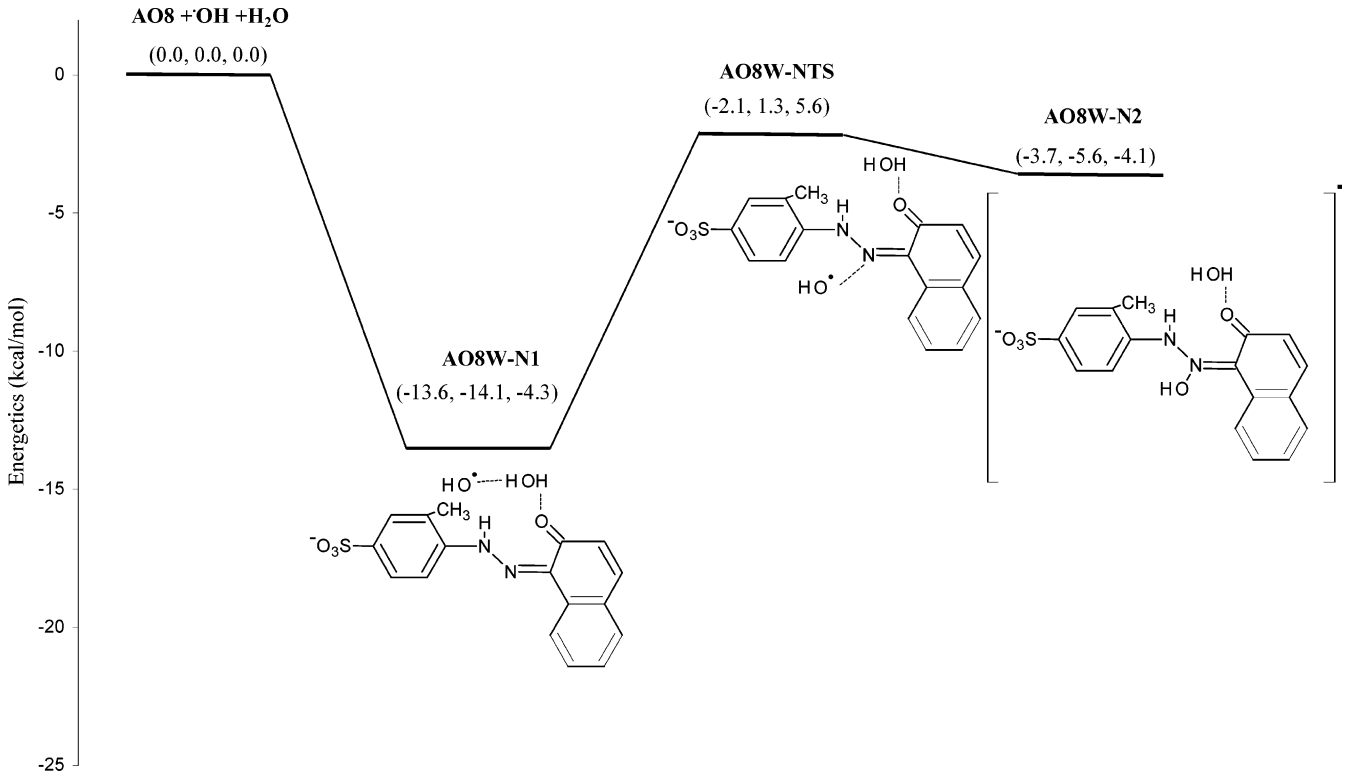

Figure 15. Potential energy profile for water-assisted H abstraction pathway of Acid Orange 8 at MPW1K/6-31G(d) level. Relative energies in parentheses are in the format of (MPW1K/6-31G(d), MPW1K/6-31+G(d,p)//MPW1K/6-31G(d), IEFPCM) values. (0.0 kcal/mol on the relative energy axis corresponds to **AO8** + •OH + H_2O = (−1615.662743, −1616.0704895, −1616.0806181) Hartrees with the same format.)

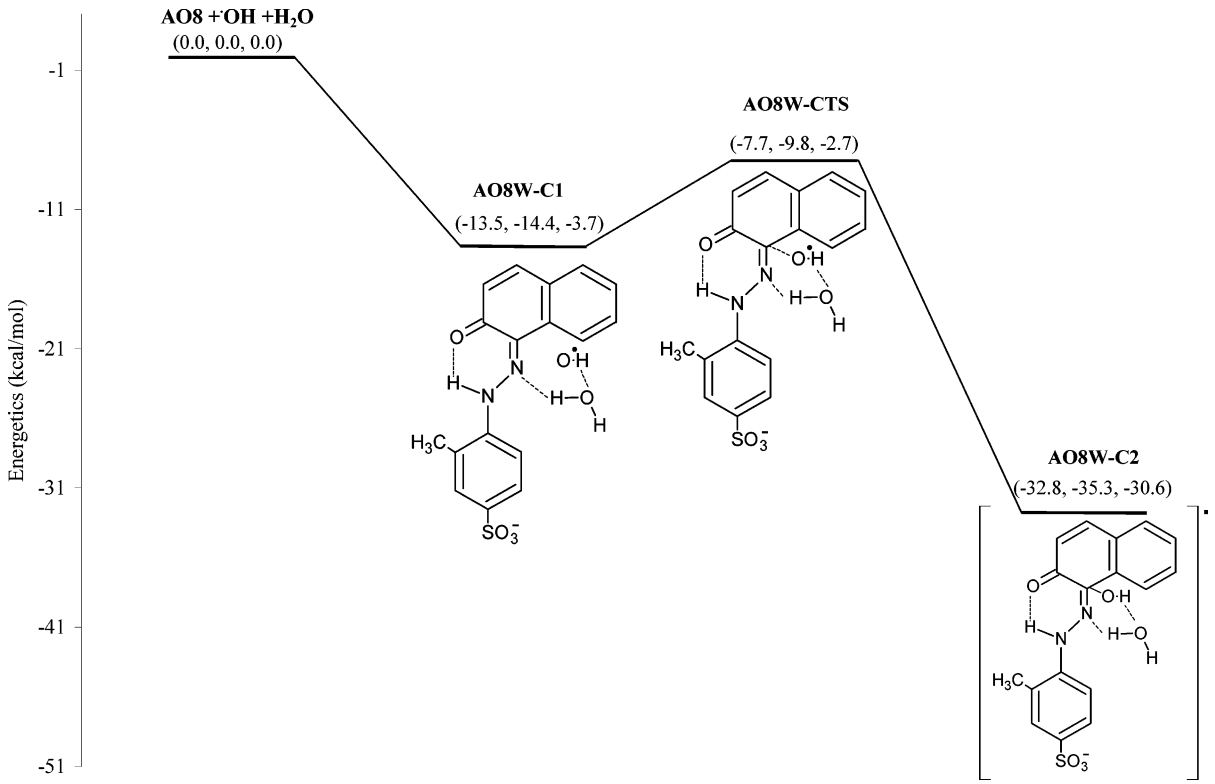

Figure 16. Potential energy profile for water-assisted C-attack pathway of Acid Orange 8 at MPW1K/6-31G(d) level. Relative energies in parentheses are in the format of (MPW1K/6-31G(d), MPW1K/6-31+G(d,p)//MPW1K/6-31G(d), IEFPCM) values. (0.0 kcal/mol on the relative energy axis corresponds to **AO8** + •OH + H_2O = (−1615.662743, −1616.0704895, −1616.0806181) Hartrees with the same format.)

the hydrogen atoms participating in hydrogen bonding and proton transfer by UFF radii since Bondi radii cavity definition was again not applicable.

Figures 3S, 4S, and 5S show the optimized structures for the water-assisted N-attack, C-attack, and H-abstraction mechanisms for AO8, respectively. The most drastic structural change due

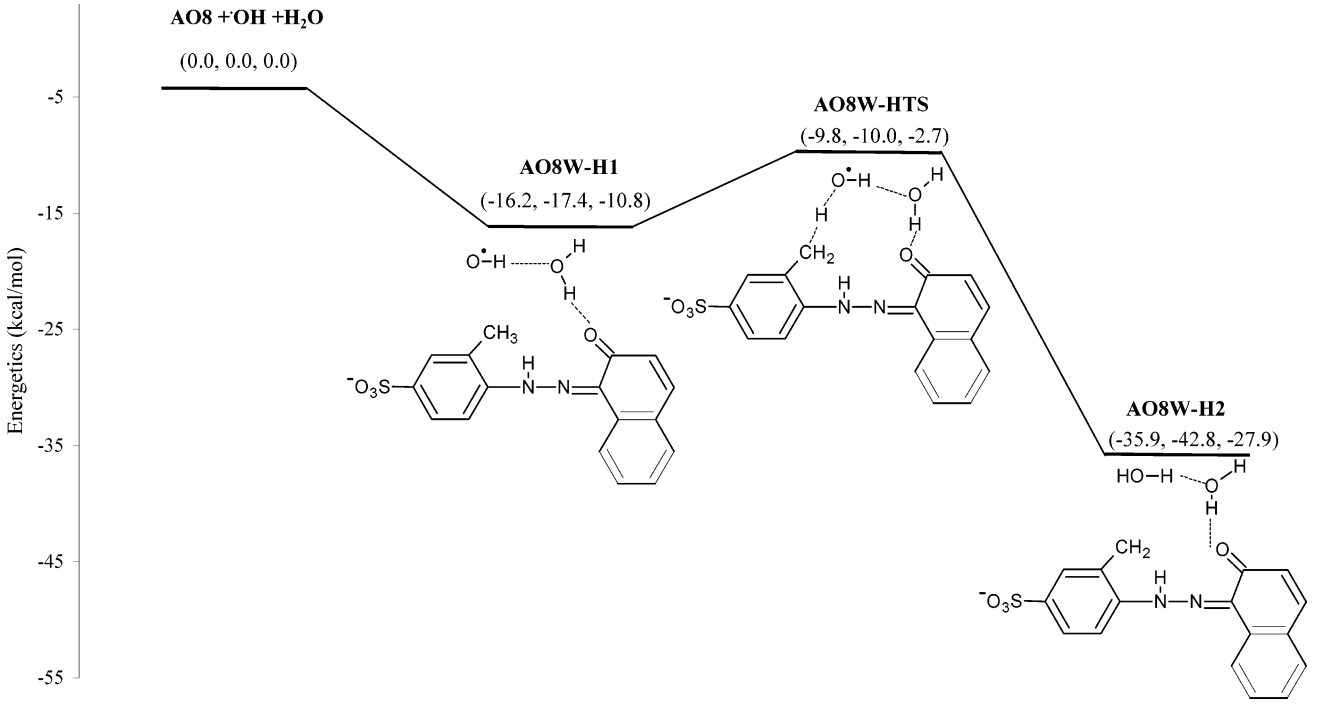

Figure 17. Potential energy profile for water-assisted H abstraction pathway of Acid Orange 8 at MPW1K/6-31G(d) level. Relative energies in parentheses are in the format of (MPW1K/6-31G(d), MPW1K/6-31+G(d,p)//MPW1K/6-31G(d), IEFPCM) values. (0.0 kcal/mol on the relative energy axis corresponds to **AO8** + •OH + H_2O = (−1615.662743, −1616.0704895, −1616.0806181) Hartrees with the same format).

to introduction of explicit water molecule has been observed in the C-attack pathway. The distance between the interacting C atom of the dye molecule and the oxygen of the hydroxyl radical shortened from 2.233 Å (**AO8**−**CTS**) to 2.056 Å (**AO8W**−**CTS**); this might be interpreted as a stronger interaction during TS, **AO8W**−**CTS**. On the other hand, the most characteristic feature of the N-attack and H-abstraction TSs (**AO8W**−**NTS** and **AO8W**−**HTS**, respectively) has been the slight lengthening of the intramolecular hydrogen bond of the dye molecule. Moreover, the shortest hydrogen bond distances between the hydrogen of the explicit water molecule and electronegative acceptor atom of the dye molecule have been observed for the H-abstraction case, because of an extra stabilization factor for this particular system. In the same context, the largest intermolecular acceptor−proton distances have been observed for the N-attack pathway.

No color removal is proposed to happen during hydrogen abstraction since the structure of the chromophore and planarity of the parent molecule is preserved. The difference between the addition and abstraction barriers is less than the difference for the *m*-substituted azo compound,[15] probably because *o*-substituted CH_3 group is sterically more hindered than the *m*-substituted one. Another reason might be the reactivity difference between the azo and hydrazone tautomers against hydroxyl radical addition reactions. As a result of the comparison of energy profiles in ref 13 with MPW1K/6-31+G(d,p)//B3LYP/6-31G(d) for azo compounds and in the present work at MPW1K/6-31+G(d,p)//MPW1K/6-31G(d) level of theory for hydrazone compounds, it can, very roughly, be estimated that the hydrazone tautomeric form is more reactive against reactions with hydroxyl radical.

Mini Benchmark: B3LYP vs MPW1K. Since the present study correlates strongly to a set of previous studies[14,15,26] and it is an extension of a more general framework on the oxidative degradation of azo dyes, B3LYP, with basis sets 6-31+(d,p) for the reactive core and 6-31G(d) for the rings, was the first choice of functional for convenience between the present and past works. However, since the potential energy of the **AO7** C-attack has a very shallow maximum, it was not possible to locate the transition state for this pathway with B3LYP and this attempt was later replaced by MPW1K functional. On the other hand, B3LYP and MPW1K give the similar trends throughout the PES even if not the same absolute energetics. A positive activation barrier was found for N-attack pathway, which is in accord with MPW1K calculations, even though the height of this barrier was underestimated by 8.3 kcal/mol (without ZPE). N-attack pathway was endoenergetic with an energy value of 2.0 kcal/mol (without ZPE) while C-attack pathway was exoenergetic with an energy value of 22.7 kcal/mol (without ZPE), in qualitative ageement with the MPW1K functional with +4.5 and −25.3 kcal/mol (without ZPE) values, respectively. Table 2 summarizes these results. Figure 18 shows the B3LYP optimized geometry of the N-attack transition-state structure together with **AO7**−**NTS**-MPW1K of Figure 5 to emphasize the resemblance. While the angles and dihedrals resemble each other in the two geometries, bond distances vary, especially for the intramolecular hydrogen bonding, probably because of the different basis sets used. In the absence of optimizations at a higher level of theory, this mini benchmark only intends to be a case study instead of deriving absolute conclusions for the use of B3LYP and MPW1K functionals in modeling the radical addition reactions.

TABLE 2: Comparison of Activation Barrier (E_a) and Reaction Energies (E_{rxn}) for B3LYP and MPW1K (without ZPE correction) kcal/mol

		B3LYP/6-31G(d) with extrabasis 6-31+G(d,p)	MPW1K/6-31G(d)
AO7 N-attack	E_a	3.3	11.6
AO7 N-attack	E_{rxn}	2.0	4.5
AO7 C-attack	E_{rxn}	−22.7	−25.3
AO8 C-attack	E_{rxn}	−21.2	−17.6

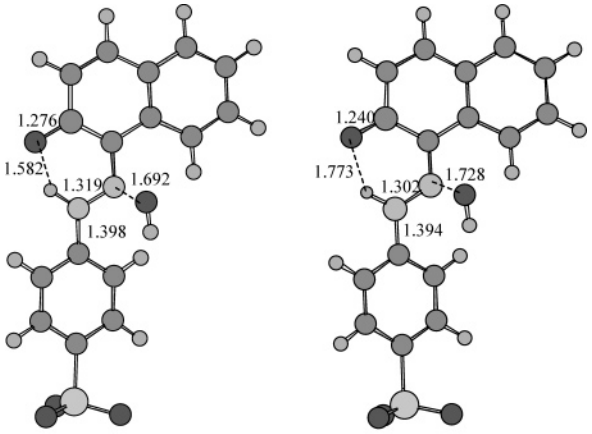

Figure 18. Comparison of the B3LYP and MPW1K optimized structures for **AO7** N-attack TS.

Conclusion

Sonochemically generated hydroxyl radicals oxidize azo dyes by pseudo-first-order reaction rates. The rate of azo dye bleaching by ultrasound is dependent on acidity and structural features among other factors. Oxidative degradation of azo dyes that exist preferably in their hydrazone forms in dye solutions follows a different mechanism than the azo tautomer degradation pathways. Adduct formation occurs through the attack of hydroxyl radical to the carbon atom bearing the azo linkage instead of the nitrogen atom. Competing reactions (like hydrogen abstraction) due to different substitutions on the rings affect the rate of color removal.

Acknowledgment. We thank Boğaziçi Üniversitesi Bilimsel Araştirma Projeleri (BAP 02B501) and Devlet Planlama Teşkilati (DPT 98K 120900) for financial support. We acknowledge the ASMA (Advanced System for Multi-computer Applications) Project at Bogazici University and also the project no 03R104 "Biyolojik Sistemler ve Polimerik Malzemelerin Modelenmesine Yönelik Üniversite Ölçekli Bilimsel Hesaplama Şebekesi Geliştirilmesi". Computational resources used in this study were partly provided by TUBITAK ULAKBIM High Performance Computing Center, which is gratefully acknowledged here.

Supporting Information Available: Potential energy surface and optimized structures for the alternative hydrogen abstraction reaction from **AO8** and optimized structures for water-assisted N-attack pathway. This material is available free of charge via the Internet at http://pubs.acs.org.

References and Notes

(1) Vinodgopal, K.; Kamat, P. V. In *Environmental Applications of Ionizing Radiation*; Cooper, W. J., Curry, R. D., O'Shea, K. E. Eds.; John Wiley & Sons: 1998; pp 587−599.
(2) Ince, N. H.; Tezcanli, G.; Belen, R. K.; Apikyan, I. G. *Appl. Catal., B: Environ.* **2001**, *29*, 167−176.
(3) Padmaja, S.; Madison, S. A. *J. Phys. Org. Chem.* **1999**, *12*, 221−226.
(4) Kuo, W. G. *Water Res.* **1992**, *26*, 881−886.
(5) Turchi, C. S.; Ollis, D. F. *J. Catal.* **1990**, *122*, 178−192.
(6) Suslick, K. S. *Science* **1990**, *247*, 1439−1445.
(7) Mason, T. J.; Lorimer, J. P.; Bates, D. M. *Ultrasonics* **1992**, *30*, 40−42.
(8) Zollinger, H. *Colour Chemistry. Synthesis, Properties and Application of Organic Dyes and Pigments*; VCH: Weinheim, Germany, 1991; pp 45−68.
(9) Kelemen, J. *Dyes Pigments* **1981**, *2*, 73−91.
(10) Kelemen, J.; Moss, S.; Sauter, H.; Winkler, T. *Dyes Pigments* **1982**, *3*, 7−47.
(11) Ball, P.; Nicholls, C. H. *Dyes Pigments* **1982**, *3*, 5−26.
(12) Joseph, J. M.; Destaillats, H.; Hung, H.; Hoffmann, M. R. *J. Phys. Chem. A* **2000**, *104*, 301−307.
(13) Spadaro, J. T.; Isabelle, L.; Renganathan, V. *Environ. Sci. Technol.* **1994**, *28*, 1389−1393.
(14) Ozen, A. S.; Aviyente, V.; Klein, R. A. *J. Phys. Chem. A* **2003**, *107*, 4898−4907.
(15) Ozen, A. S.; Aviyente, V.; De Proft, F.; Geerlings, P. *J. Phys. Chem. A* **2004**, *108*, 5990−6000.
(16) Sullivan, A. G.; Garner, R.; Gaskell, S. J. *Rapid Commun. Mass Spectrom.* **1998**, *12*, 1207−1215.
(17) Ince, N. H.; Tezcanli-Guyer, G. *Ultrasonics* **2004**, *42*, 591−596.
(18) Galindo, C.; Jacques, P.; Kalt, A. *J. Adv. Oxid. Technol.* **1999**, *4*, 400−407.
(19) Frisch, M. J.; Trucks, G. W.; Schlegel, H. B.; Scuseria, G. E.; Robb, M. A.; Cheeseman, J. R.; Zakrzewski, V. G.; Montgomery, J. A., Jr.; Stratmann, R. E.; Burant, J. C.; Dapprich, S.; Millam, J. M.; Daniels, A. D.; Kudin, K. N.; Strain, M. C.; Farkas, O.; Tomasi, J.; Barone, V.; Cossi, M.; Cammi, R.; Mennucci, B.; Pomelli, C.; Adamo, C.; Clifford, S.; Ochterski, J.; Petersson, G. A.; Ayala, P. Y.; Cui, Q.; Morokuma, K.; Malick, D. K.; Rabuck, A. D.; Raghavachari, K.; Foresman, J. B.; Cioslowski, J.; Ortiz, J. V.; Baboul, A. G.; Stefanov, B. B.; Liu, G.; Liashenko, A.; Piskorz, P.; Komaromi, I.; Gomperts, R.; Martin, R. L.; Fox, D. J.; Keith, T.; Al-Laham, M. A.; Peng, C. Y.; Nanayakkara, A.; Gonzalez, C.; Challacombe, M.; Gill, P. M. W.; Johnson, B.; Chen, W.; Wong, M. W.; Andres, J. L.; Gonzalez, C.; Head-Gordon, M.; Replogle, E. S.; Pople, J. A. *Gaussian 98*, Revision A.7; Gaussian, Inc.: Pittsburgh, PA, 1998.
(20) Lynch, B. J.; Fast, P. L.; Harris, M.; Truhlar, D. G. *J. Phys. Chem. A* **2000**, *104*, 4811.
(21) Tomasi, J.; Mennucci, B.; Cancés, E. *J. Mol. Struct. (THEOCHEM)* **1999**, *464*, 211−226.
(22) Oakes, J.; Gratton, P. *J. Chem. Soc., Perkin Trans.* **1998**, *2*, 1857−1864.
(23) Tezcanli-Guyer, G.; Ince, N. H. *Ultrasonics* **2004**, *42*, 603−609.
(24) Tezcanli-Guyer, G.; Alaton, I. A.; Ince, N. H. *Coloration Technol.* **2003**, *119*, 292−296.
(25) Bader, R. F. W. *Atoms in Molecules: A Quantum Theory International Series of Monographs on Chemistry*; Clarendon Press: Oxford, 1995; Vol. 22, pp 1−43.
(26) Ozen, A. S.; Aviyente, V.; Doruker, P. *J. Org. Chem.*, to be submitted for publication.
(27) Takeda, S.; Tanaka, Y.; Nishimura, Y.; Yamane, M.; Siroma, Z.; Wakida, S. *J. Chromatogr., A* **1999**, *853*, 503−509.
(28) Hustert K.; Zepp R. G. *Chemosphere* **1992**, *24*, 335−342.